Available online at www.sciencedirect.com
ScienceDirect
Trans. Nonferrous Met. Soc. China 31(2021) 1059−1073
Transactions of
Nonferrous Metals
Society of China
www.tnmsc.cn

Displacive transformation as pathway to prevent micro-cracks induced by thermal stress in additively manufactured strong and ductile high-entropy alloys

Rui-di LI[1], Peng-da NIU[1], Tie-chui YUAN[1], Zhi-ming LI[1,2]

1. State Key Laboratory of Powder Metallurgy, Central South University, Changsha 410083, China;
2. School of Materials Science and Engineering, Central South University, Changsha 410083, China

Received 19 May 2020; accepted 18 December 2020

Abstract: The micro-cracking behaviors of two high-entropy alloys (HEAs) of the FeMnCoCrNi family prepared by selective laser melting were systematically studied. Residual stresses were also analyzed by X-ray diffraction technique. Results show that the equiatomic FeMnCoCrNi HEAs with a relatively stable single-phase face-centered cubic (FCC) structure suffered from micro-cracking with residual tensile stress after laser melting. In contrast, the metastable non-equiatomic FeMnCoCr HEAs with reduced stacking fault energy are free of micro-cracks with residual compressive stress at various volumetric energy densities (VEDs). The displacive transformation from the FCC matrix to the hexagonal close-packed (HCP) phase during cooling prevents the micro-cracking via consuming thermal stress related internal energy. Further, the displacive transformation during tensile deformation contributes to the higher strength and ductility of the metastable dual-phase HEA compared to that of the stable single-phase HEA. These findings provide useful guidance for the design of strong, ductile, and crack-free alloys for additive manufacturing by tuning phase stability.

Key words: selective laser melting; high-entropy alloys; phase transformation; micro-cracking; residual stress

---

1 Introduction

Additive manufacturing (AM) is now attracting significant interests from both academic and industrial fields owing to its flexible manufacturing of 3D near-net-shape parts in cost effective and material saving manners [1−3]. As one of the powder bed fusion processes of AM, the selective laser melting (SLM) is increasingly used for manufacturing of metallic parts in a successive lay-by-layer fashion with fine microstructures and complex shapes [4]. Although fabricating fully dense components using SLM is an area of great interest, it faces significant challenges of micro-cracking in many processed alloys. The micro-cracking behavior is generally related to the thermal stress induced during SLM, which is sometimes also coupled with the micro-pores formed at the late state of solidification during laser melting [1,5−8]. In this regard, a large number of conventional high-strength alloys are not suited for SLM and other laser AM techniques as micro-cracking behavior deteriorates the mechanical properties of the printed alloys. Therefore, the micro-crack associated with the thermal stresses in 3D printed metal parts has been one of the most critical issues for metal AM.

In order to fabricate crack-free AM metal components, several methods have been employed to eliminate the cracks during or after AM process. First, the hot isostatic pressing (HIP) has been used to consolidate cracks in the alloys prepared by AM [9,10]. However, the open porosity and surface

---

Corresponding author: Zhi-ming LI; Tel: +86-13687308769; E-mail: lizhiming@csu.edu.cn
DOI: 10.1016/S1003-6326(21)65561-9

cracks still remain after HIP [11]. Also, HIP usually gives rise to grain growth, leading to coarser grains and lower strength of the AM metal parts. Second, optimizing the 3D printing parameters, such as laser power, scan speed, layer thickness and scanning strategy, has also been employed to alleviate the residual tensile stress and associated cracks [12−15]. Yet, the optimization of processing parameters can only be probed in a certain extent and micro-cracking can still occur particularly in crack-susceptive alloys. Third, preheating of substrate prior to 3D printing has been tried to reduce the thermal stresses. However, the preheating temperature is usually low (below 250 °C) since high preheating temperature is detrimental for AM metal parts [16−18]. In this context, the reduction in thermal stresses by preheating substrate is limited. Also, the preheating of substrate could not alleviate the thermal stresses in layers deposited relatively far away from the substrate. Fourth, adjusting minor alloying elements in crack-sensitive alloys to tailor the solidification path or refine the primary phase has been studied to relieve the micro-cracking in AM metal parts. For instance, lowering the contents of Mn and C has been found to help in avoiding cracks in SLM printed Hastelloy X alloy due to the reduced interdendritic brittle phases [5]. Adding Si can effectively suppress the micro-cracks in the SLM printed Al−Zn−Mg−Cu alloy [19−21] by eutectic filling and adding Zr can eliminate the micro-cracks in the SLM printed Al2024 alloy by grain refinement [22−24]. Despite that various approaches have been utilized to relieve the formation of cracks in AM metal parts, the residual tensile stresses and the associate cracking issues in 3D printed alloys are still presented commonly.

The concept of high-entropy alloys (HEAs) is currently also arousing widespread interest owing to its inherent immense compositional variability for designing the new materials with the excellent mechanical, physical and chemical properties [25−28]. Several HEA systems have been probed over the past fifteen years, such as face-centered cubic (FCC) FeMnCoCrNi system [29,30], body-centered cubic (BCC) TiNbTaZrHf system and other dual- or multi-phase alloy systems [31,32]. Some of them show promising properties, e.g., exceptional cryogenic fracture toughness [33] and high resistance to hydrogen embrittlement [34,35] have been revealed in the FeMnCoCrNi HEA. Recently, additive manufacturing techniques have also been employed to synthesize bulk HEAs. In fact, one of the advantages of SLM for HEAs is that the rapid solidification within the melt pool could facilitate the formation of supersaturated solid solutions with ultra-fine grains [36,37]. So far, AM of HEAs has been widely studied [38−40]. However, similar to the cases of conventional alloys introduced above, most of HEAs, such as the FCC CoCrFeMnNi, FCC CoCrFeNi and BCC AlCoCrFeNi, have also suffered from cracking when they were printed by SLM [41−47].

In fact, nucleation and propagation of micro-cracks can be considered as possible ways of dissipating internal energy related to thermal stress in the materials. In this regard, we introduce other pathways rather than crack nucleation and propagation to absorb the internal energy, and hence to prevent micro-cracking of the alloys produced by AM. In the present study, we suggest that rendering in-situ displacive phase transformation to consume the internal energy induced by thermal tensile stress during SLM is effective to prevent the micro-cracking in metastable HEAs. To demonstrate our concept, in the following we show the SLM processing, morphology, microstructure and deformation behavior of a representative metastable HEA ($Fe_{50}Mn_{30}Co_{10}Cr_{10}$, at.%) comparing with that of a relatively stable FCC HEA ($Fe_{20}Mn_{20}Co_{20}Cr_{20}Ni_{20}$, at.%). Although the compositions of the stable equiatomic FeMnCoCrNi HEA and the metastable non-equiatomic FeMnCoCr HEA are not exactly the same, the present work provides the new insights that phase stability of HEAs can be properly reduced by tuning the compositions to trigger displacive transformation and thereby prevent micro-cracking caused by the residual thermal stresses.

2 Experimental

2.1 Selective laser melting

Two different HEAs of the FeMnCoCrNi family, i.e., the stable single FCC phase $Fe_{20}Mn_{20}Co_{20}Cr_{20}Ni_{20}$ (at.%) and the metastable dual-phase $Fe_{50}Mn_{30}Co_{10}Cr_{10}$ (at.%) were selected for the SLM processing. Powders of the two HEAs were prepared by gas atomization with the following steps. Firstly, the pure metals (Fe, Mn, Co, Cr and Ni) with high purity (≥99.9%) were melted at 1500 °C in an induction heated vacuum furnace. Then, the molten liquid metal was sprayed through Al_2O_3 ceramic tube with the nozzle hole diameter of 3.5 mm under high-purity (≥99.9%) Ar atmosphere at 4 MPa. Finally, the obtained powders were then sieved to have a size distribution range of 5−45 μm. The particle size was measured using a laser particle size analyzer (Matersizer). The as-prepared powders show spherical shape according to the scanning electron microscopy (SEM) analysis. The chemical compositions of the powders were measured by the inductively coupled plasma atomic emission spectrometry (ICP-AES) and the results are shown in Table 1.

SLM processing was performed at room temperature using an FS271 facility (Farsoon, Inc, China) equipped with a 500 W Gaussian beam fiber laser with a focal laser beam diameter of 90 μm under high purity Ar atmosphere. A grit-blasted stainless-steel plate was used as the substrate of powder deposition. After the SLM processing, the printed HEA parts and the steel substrate were separated by using the electrical discharge machining.

Cubic samples with dimensions of 10 mm × 10 mm × 10 mm were first printed with different SLM parameters to obtain the optimal parameters. Using the optimized parameters, larger blocks with dimensions of 80 mm × 10 mm × 10 mm were produced. The SLM parameters used in the present study were: laser power (*P*) 400 W, scan speed (*v*) 800−1600 mm/s, scan interval (*h*) 0.09 mm, and layer thickness (*t*) 30 μm. Volumetric energy density (VED) can be estimated based on the SLM parameters (*P*, *v*, *t*, *h*), i.e., VED=$P/(vht)$. In the present study, to better compare the printability, micro-cracking behavior and microstructural evolution of the two HEAs from the FeMnCoCrNi family, the same VEDs (SLM parameters) were used for the two alloys, i.e., 185.2, 123.5 and 92.6 J/mm^3, respectively.

2.2 Microstructural and mechanical characterization

The relative density of the SLM printed samples was tested by the Archimedean method. Phase identification was conducted by a D/max2500pc X-ray diffractometer (XRD) with Cu K_α radiation (λ=0.15406 nm). For microstructural analysis, sample surfaces were ground and polished, and then etched with a solution consisting of H_2O_2 (10 mL), HCl (16 mL) and methyl alcohol (24 mL). The morphologies of the etched sample surfaces were observed by an optical microscope (OM, Leica DM2700P, Germany). Scanning electron microscopy (SEM) analysis and electron backscatter diffraction (EBSD) measurements were performed using a FEI NanoLab 600i microscope equipped with a NordlysMax^3 camera and the Oxford channel 5 data collection software. Transmission electron microscopy (TEM) investigations were performed using a JEOL 2100F microscope operated at 200 kV. The microscale elemental distributions in the SLM printed samples were analyzed with an Electron Probe Micro Analyzer (EPMA) (JXA−8530, JEOL, Japan). Also, the nanoscale elemental distributions were investigated using atom probe tomography (APT) (LEAP 3000X HR, Cameca Inc.). APT tips were prepared using the focused ion beam (FIB) technique (FEI Helios Nanolab 600i). The residual stress measurements were carried out on the surfaces of the printed alloy parts with different compositions using the X-ray sin 2ψ technique by an X-ray tube (XStress3000) operated at 30 kV and 6.7 mA with 18 different interplanar angles (ψ) from −45° to 45°. The diffraction angle (2θ) was 142°−156°. The residual stress was calibrated with elastic strain theory according to the Hook's law using austenitic stainless, and the elastic modulus and Poisson ratio are 196 GPa and 0.28, respectively. Each sample was tested three times to confirm the data reproducibility.

Dog-bone-shaped tensile specimens with a

Table 1 Chemical compositions of atomized powders measured by inductively coupled plasma atomic emission spectrometry (ICP-AES) (at.%)

Alloy	Mn	Co	Cr	Ni	Si	Zr	C	O	S	P	Fe
$Fe_{20}Mn_{20}Co_{20}Cr_{20}Ni_{20}$	20.1	18.3	18.9	18.6	<0.001	<0.00001	<0.0002	0.0032	0.00025	<0.0001	Bal.
$Fe_{50}Mn_{30}Co_{10}Cr_{10}$	28.2	9.44	9.89	0.0008	<0.001	<0.00001	<0.0002	0.003	0.00019	0.00016	Bal.

thickness of 3 mm and a total length of 80 mm were machined from the SLM printed blocks by electrical discharge machining. The gauge length and width were 25 and 3 mm, respectively. Uniaxial tensile tests were performed on an MST Alliance RT machine (MTS systems, Eden Prairie, MN, USA) at a crosshead speed of 2 mm/min at room temperature, i.e., an initial strain rate of 1.3×10^{-3} s^{-1}. The deformed microstructures in the tensile tested samples were also investigated by SEM-EBSD and TEM.

3 Results

3.1 Phase constitutions of as-printed alloys

Figure 1 shows the XRD patterns of the quaternary non-equiatomic $Fe_{50}Mn_{30}Co_{10}Cr_{10}$ (at.%) and equiatomic quinary FeMnCoCrNi HEAs printed at different volumetric energy densities (VEDs) by SLM. The equiatomic FeMnCoCrNi HEA shows a single FCC γ phase after printing at varying VEDs. In contrast, the non-equiatomic $Fe_{50}Mn_{30}Co_{10}Cr_{10}$ (at.%) HEA contains both FCC γ and HCP ε phases. Further, the volume fraction of HCP ε phase increases with increasing the VED according to the increased intensities of diffraction peaks of HCP ε phase.

3.2 Micro-cracking behavior in as-printed HEAs

Figure 2 shows the optical micrographs of the as-printed HEAs from the cross-sections and vertical-sections at different VEDs. For the single-phase equiatomic FeMnCoCrNi HEA, a large number of micro-cracks with an average length of ~10 μm can be observed in samples with varying VEDs. This suggests that the stable single-phase equiatomic FeMnCoCrNi HEA is susceptible upon AM by SLM. Interestingly, the as-printed metastable dual-phase non-equiatomic $Fe_{50}Mn_{30}Co_{10}Cr_{10}$ (at. %) HEA is totally crack-free at varying VEDs. This is related to the displacive transformation from the FCC matrix to the HCP phase during SLM process.

The microstructure of the SLM printed $Fe_{50}Mn_{30}Co_{10}Cr_{10}$ (at.%) HEA revealed by optical micrographs in Figs. 2(d−f) shows a typical stripe structure in the cross-sections and an overlap structure in the vertical-sections. From the micrographs of the cross-sections, the weld tracks are overlapped and their shapes are irregular. From the micrographs of the horizontal cross-section, the scan tracks can be clearly observed, and the angle between the laser scanning direction and the consecutive layers is ~67°. For both the two HEAs, the relative density of the as-printed samples gradually increases with increasing the VED according to the Archimedean method. At the highest VED (i.e., 185.2 J/m^3), the relative density of the dual-phase $Fe_{50}Mn_{30}Co_{10}Cr_{10}$ (at.%) and single-phase equiatomic FeMnCoCrNi HEAs are 99.8% and 98.2%, respectively. Also, some spherical particles are presented in the melt pools. They are inclusions enriched in Mn and hard to be avoided in high Mn-containing alloys [48,49].

3.3 Residual stress in as-printed alloys

Figure 3 shows the measured residual stresses of the additively manufactured equiatomic

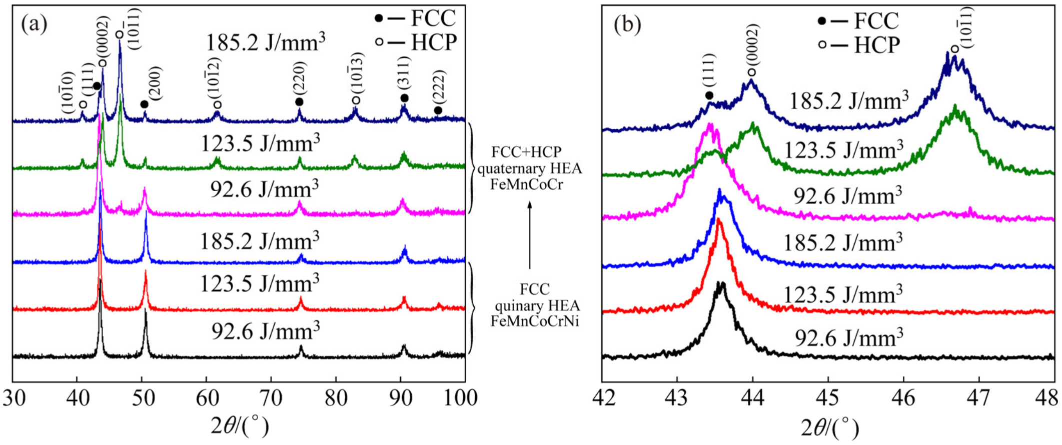

Fig. 1 XRD analysis of SLM processed equiatomic FeMnCoCrNi and non-equiatomic $Fe_{50}Mn_{30}Co_{10}Cr_{10}$ (at.%) HEAs: (a) XRD patterns of two types of HEAs printed at different VEDs; (b) Zoom-in images of patterns with 2θ ranging from 42° to 48°

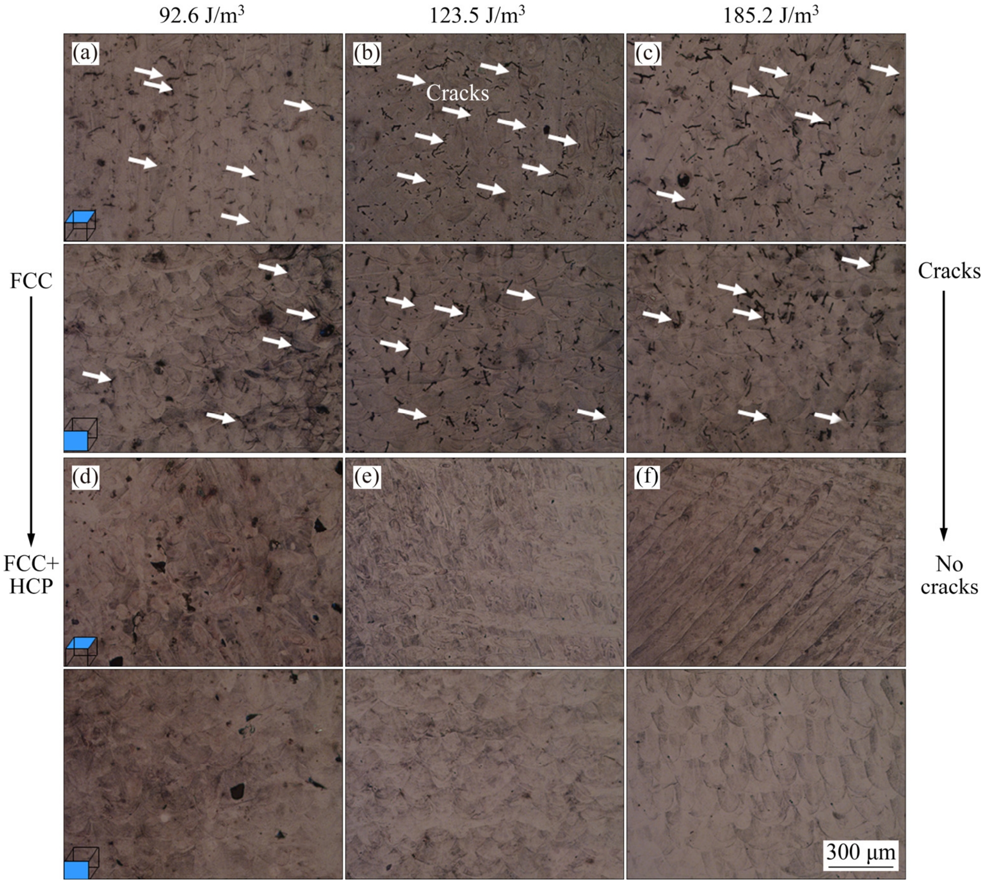

Fig. 2 Optical micrographs showing cross-sections and vertical-sections of SLM printed HEAs at different VEDs: (a−c) Single-phase equiatomic FeMnCoCrNi; (d−f) Dual-phase non-equiatomic $Fe_{50}Mn_{30}Co_{10}Cr_{10}$ (at.%)

FeMnCoCrNi and non-equiatomic $Fe_{50}Mn_{30}Co_{10}Cr_{10}$ HEAs at different VEDs. The SLM processed single-phase equiatomic FeMnCoCrNi HEA samples show tensile stresses at the different VEDs, while compressive stresses were detected in the dual-phase non-equiatomic $Fe_{50}Mn_{30}Co_{10}Cr_{10}$ HEA samples under the same processing parameters. This suggests that the residual stress transformed from tensile stress in stable single-phase HEA to compressive stress in metastable dual-phase HEA, which is related to the partial martensitic phase transformation in the metastable HEA. The occurrence of residual compressive stress in the metastable HEA can be ascribed to the slight volume expansion with the increase of phase interfaces and defects accompanying the phase transformation. Generally, tensile stress can lead to micro-cracking behavior in additively manufactured alloys during the fast cooling process [50], while the micro-cracks are absent from the compressive stress condition [51]. Further, both the residual tensile stress in the stable single-phase HEA and the residual compressive stress in the metastable dual-phase HEA gradually increase with the increase of VED, as shown in Fig. 3. This is related to the much higher melt pool temperature and faster cooling rate at higher VEDs.

3.4 Microstructure and elemental distribution

Figure 4 shows the typical microstructures of the SLM printed single-phase equiatomic quinary FeMnCoCrNi and dual-phase non-equiatomic quaternary $Fe_{50}Mn_{30}Co_{10}Cr_{10}$ (at.%) HEAs. Similar to that shown in the optical images in Fig. 2, the quinary equiatomic FeMnCoCrNi HEA exhibits micro-cracks at the melt pool boundaries and inside the melt pools (Figs. 4(a−c)). However, in the quaternary $Fe_{50}Mn_{30}Co_{10}Cr_{10}$ (at.%) HEA, no cracks were found at any VEDs (Figs. 4(d−f)). Also, the melt-pool boundaries of both the single- and dual phase alloys are clear. For single-phase HEA, the micro-cracking occurs mainly at high angle grain boundaries. Further observation of the microstructure shows fine columnar and cellular

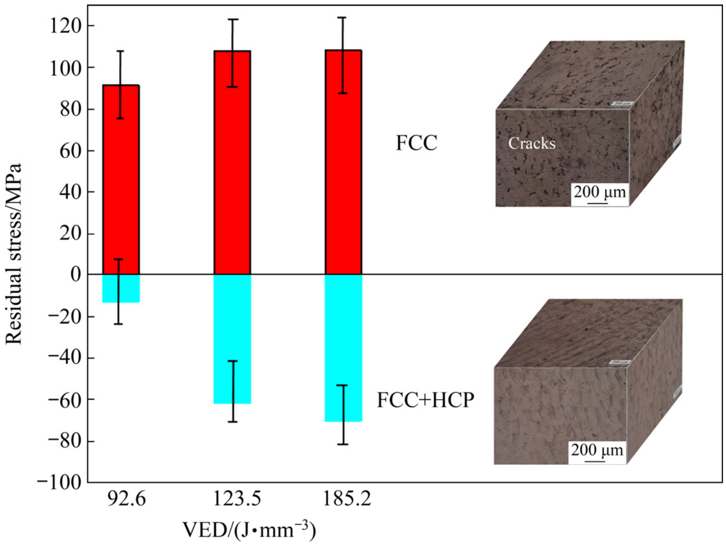

Fig. 3 Residual stresses in as-printed single-phase equiatomic FeMnCoCrNi and dual-phase non-equiatomic $Fe_{50}Mn_{30}Co_{10}Cr_{10}$ (at.%) HEAs at different VEDs

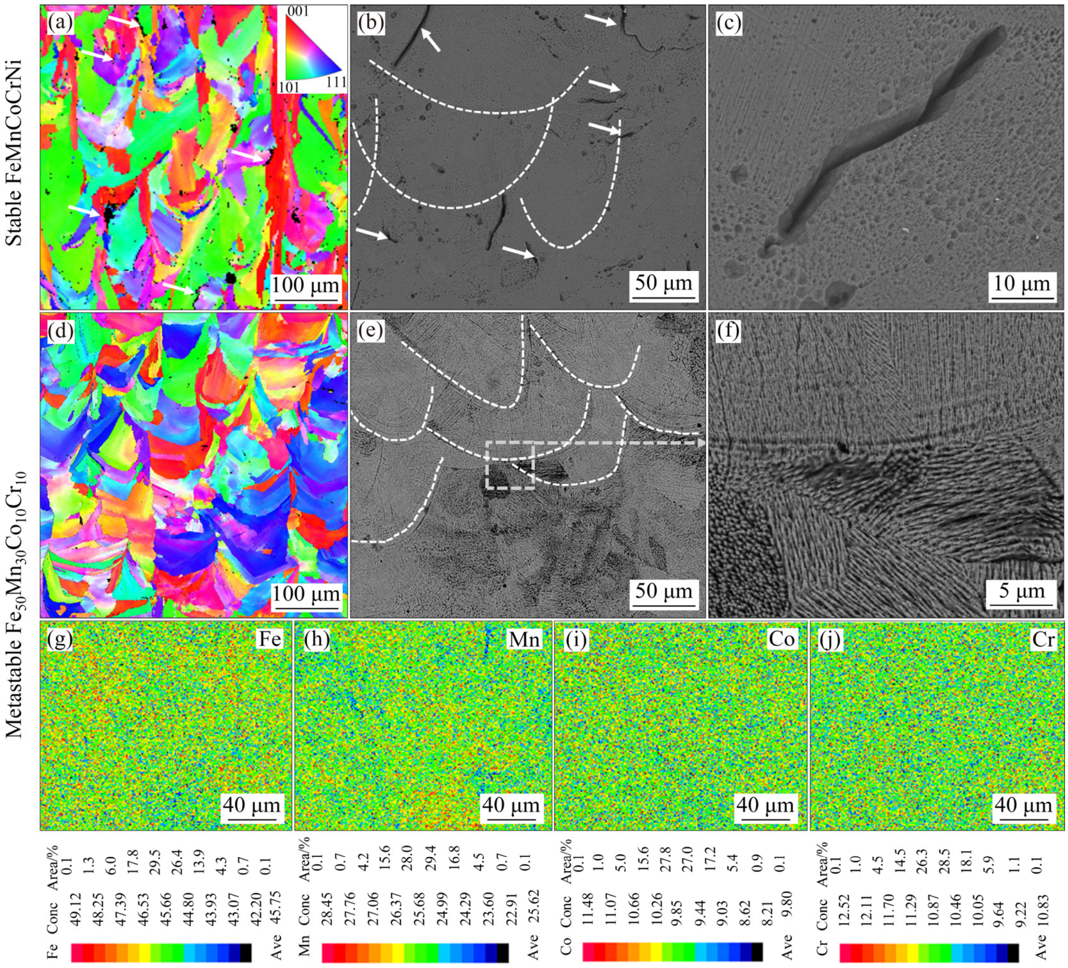

Fig. 4 Microstructures and elemental distributions of as-printed HEAs: (a) EBSD IPF map; (b, c) SEM images of single-phase equiatomic FeMnCoCrNi HEA; (d) EBSD IPF map; (e, f) SEM images of dual-phase non-equiatomic $Fe_{50}Mn_{30}Co_{10}Cr_{10}$ (at.%) HEA; (g−j) Elemental distribution maps of Fe, Mn, Co and Cr in as-printed dual-phase non-equiatomic $Fe_{50}Mn_{30}Co_{10}Cr_{10}$ (at.%) HEA obtained from EPMA analysis (The microstructural observation plane is parallel to the building direction. The white arrows in (b) indicate the micro-cracks, and the white dashed lines refer to the melt pool boundaries)

grains. Bundles of these grains in the consecutive layers follow the same direction, indicating the epitaxial growth. In the process of grain growth, the “easy growth” direction (the ⟨100⟩ of the FCC crystal structure) is dependent on the thermal dissipation direction. In order to reveal the grain texture, the IPF images of the single FCC and dual FCC+HCP samples printed by SLM were provided in Figs. 4(a) and (d), respectively. From the cross-sections of the samples, it can be seen that the melt pools were accumulated layer by layer. The elongated grains are often blocked at the solidification front, forming new grains with random crystallographic orientation and resulting in more isotropic grain characteristics after SLM. In order to analyze the elemental distribution of the quaternary $Fe_{50}Mn_{30}Co_{10}Cr_{10}$ (at.%) HEA, EPMA maps of Fe, Mn, Co and Cr were collected from the sample section parallel to the building direction, as shown in Figs. 4(g−j). All the alloy elements are homogeneously distributed in the side view of the as-printed sample.

We also conducted TEM analysis to further reveal the nano-scale microstructure, as shown in Fig. 5. From the TEM bright field images (Figs. 5(a, b, d, e)), high density dislocations are present in both the stable and metastable HEAs. This also suggests the presence of residual stresses caused by the rapid solidification during SLM. There is also a high number density of stacking faults (SFs) in the as-built metastable $Fe_{50}Mn_{30}Co_{10}Cr_{10}$ HEA due to its low SF energy (~6.5 mJ/m^2) [52]. HCP laminates with thickness ranging from 20 to 500 nm are also captured in the

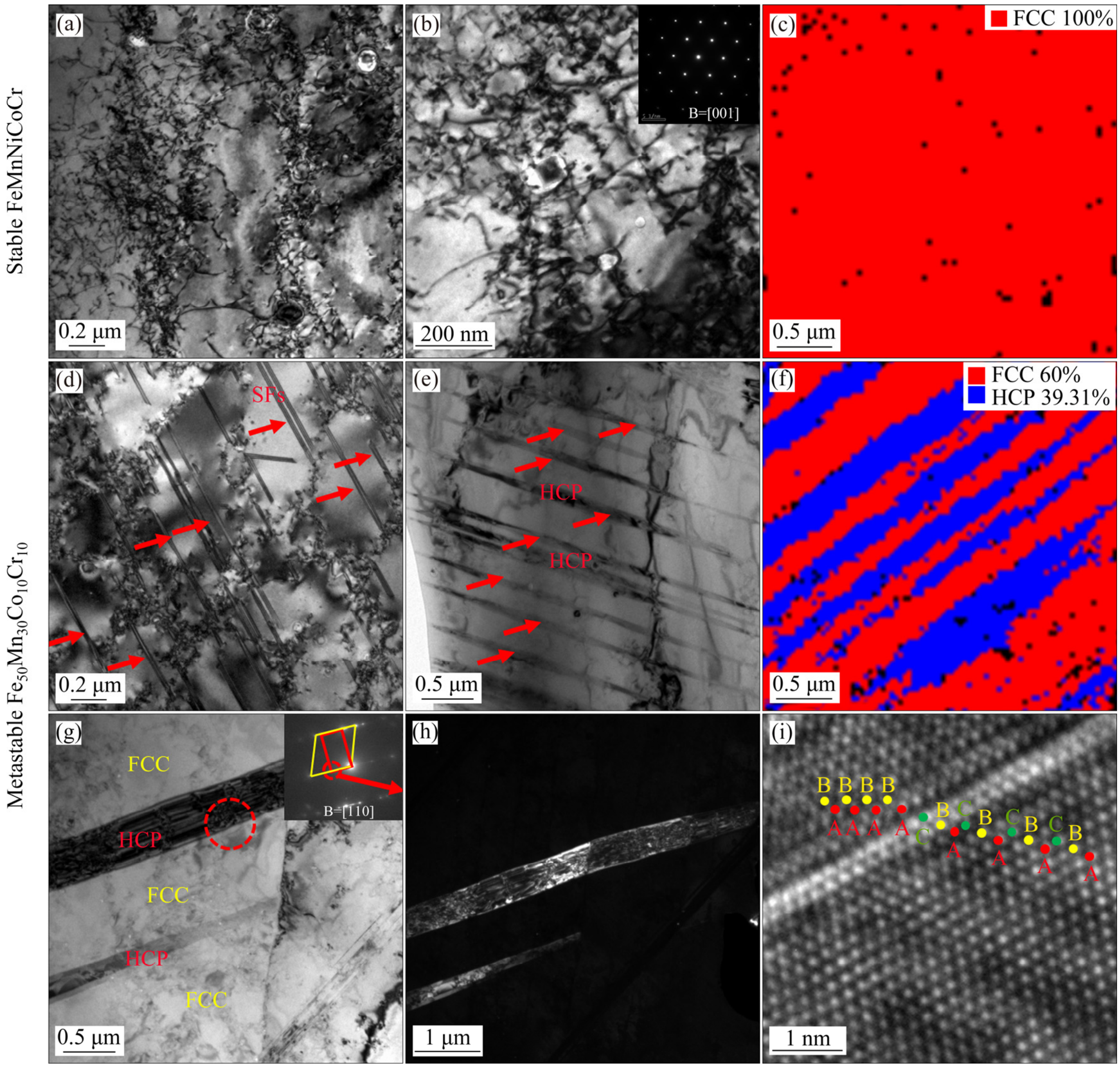

Fig. 5 Microstructures of different HEAs prepared by SLM: (a, b) TEM images with different magnifications; (c) EBSD phase map; (d, e, g) TEM bright field image; (f) EBSD phase map; (h) Corresponding dark field image; (i) HRTEM image of interface between HCP phase and FCC matrix

as-built metastable HEA by TEM observation (Fig. 5(e)) and transmission EBSD analysis (Fig. 5(f)). Figures 5(g) and (h) display the bright field and dark field TEM images of the typical microstructure in the SLM printed metastable dual-phase HEA, respectively, which further illustrates the co-existence of HCP and FCC phases. According to the atomic columns shown in Fig. 5(i), there is a standard S−N orientation relationship between the HCP phase and the FCC matrix, i.e., $\langle 11\bar{2}0\rangle_{\mathrm{HCP}}//\langle 110\rangle_{\mathrm{FCC}}$ and $(0002)_{\mathrm{HCP}}//\{111\}_{\mathrm{FCC}}$ [52]. Also, the uniform Z-contrast of the two phases shows no apparent atomic scale composition modulation.

In order to check the nanoscale elemental distribution and the exact local composition in the metastable $\mathrm{Fe_{50}Mn_{30}Co_{10}Cr_{10}}$ HEA, the APT tips were lifted out for analysis, and the representative results are shown in Fig. 6. The 3D-APT tip reconstruction of all the elements in the representative tip shows that there is no apparent elemental segregation in the probed volume (Fig. 6(a)). The one-dimensional compositional profiles (Fig. 6(b)) show that there is no obvious fluctuation of the elemental composition along the length direction of the tip, and the analysis reveals that the tip of the quaternary HEA has an overall composition of $\mathrm{Fe_{52.79}Mn_{24.44}Co_{11.39}Cr_{11.38}}$ (at.%). Further, the statistical binomial frequency distribution analysis shows that the experimental

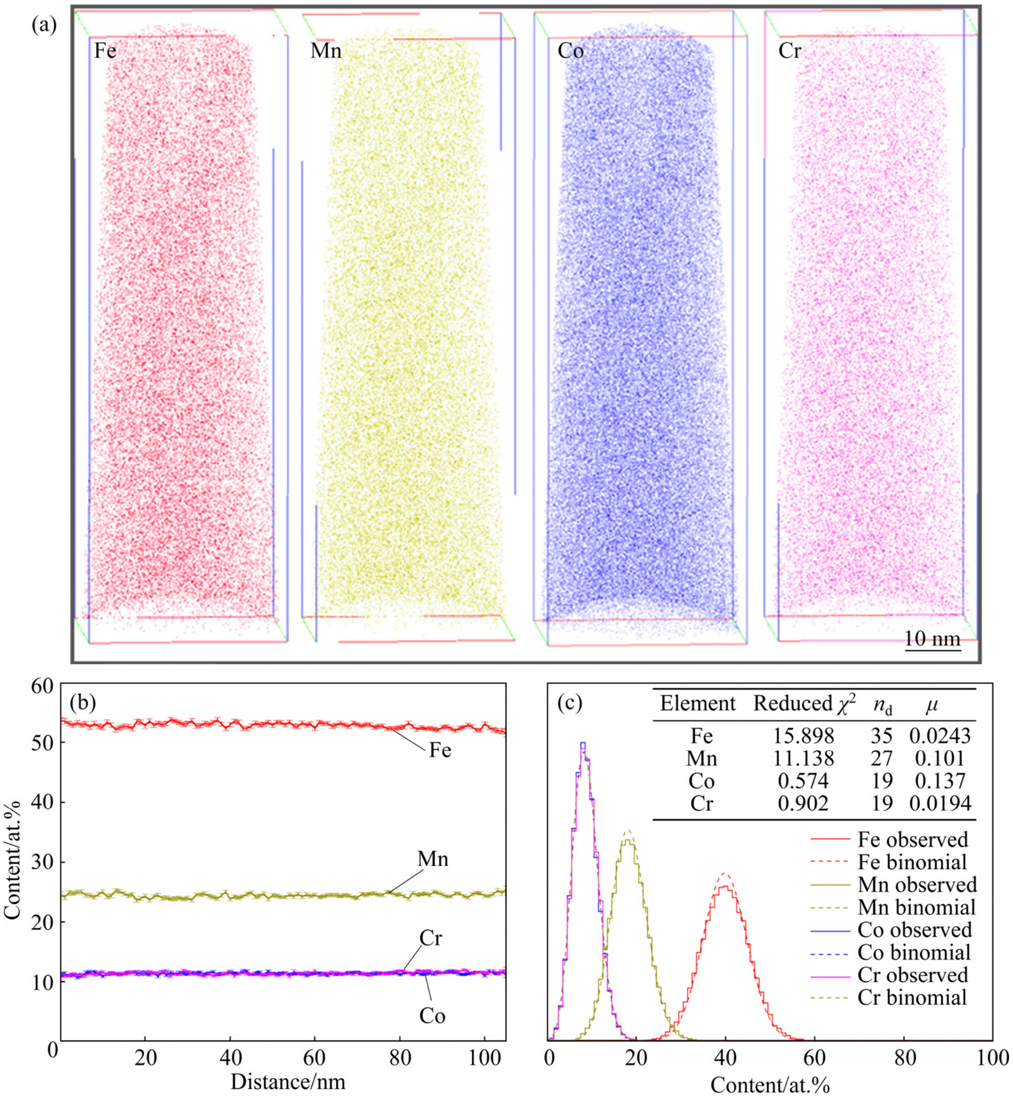

Element	Reduced χ^2	n_d	μ
Fe	15.898	35	0.0243
Mn	11.138	27	0.101
Co	0.574	19	0.137
Cr	0.902	19	0.0194

Fig. 6 Representative APT analysis of SLM processed $\mathrm{Fe_{50}Mn_{30}Co_{10}Cr_{10}}$ HEA: (a) 3D-APT tip reconstruction of different elements; (b) One-dimension compositional profiles taken along length direction of tip; (c) Frequency distribution analysis from experimental results and binominal simulation (Several parameters were used to evaluate the fitting quality, as shown in the Table inserted in (c). n_d and μ are the degrees of the freedom for a given ion and the normalized homogenization parameter, respectively)

binomial curve is in good agreement with the curve corresponding to the complete random distribution (Fig. 6(c)). The normalized homogenization parameter (μ) is close to 0 for the four elements, confirming the random distribution of all elements (Fe, Mn, Co and Cr). Therefore, effects of segregation and precipitation in both micro- and nano-scales on the properties of the material can be ruled out based on the above EPMA and APT analysis.

3.5 Mechanical properties and deformation microstructure

Figure 7(a) shows the representative engineering stress−strain curves of the SLM samples at different VEDs. Both the yield stress and ultimate tensile stress are enhanced with the increase of VED from 92.6 to 123.5 J/mm^3. At VED of 185.2 J/mm^3, the highest ultimate tensile strength of 776 MPa and elongation of 26% were obtained. The enhanced tensile properties with increasing VED is related to the fact that the increase of VED favors the densification of the as-printed samples (Figs. 2(d−f)). At the relatively low VED of 92.6 J/mm^3, a large number of pores are visible, thus the strength and ductility are significantly weakened. With the increase of VED to 185.2 J/mm^3, the densification of the as-printed samples is highly improved, thus the tensile strength and ductility are increased.

Figures 7(b−d) show the EBSD maps of the regions with different local strain levels (20%, 25% and 30%) in the tensile tested sample at the VED of 185.2 J/mm^3. It is clear that more HCP martensite is formed in the FCC matrix with increasing the strain levels. Specifically, the phase fractions of HCP martensite at strain levels of 20%, 25% and 30% are 63.1%, 78.8% and 80.2%, respectively. This suggests the dynamic displacive transformation from the FCC matrix to the HCP martensite during

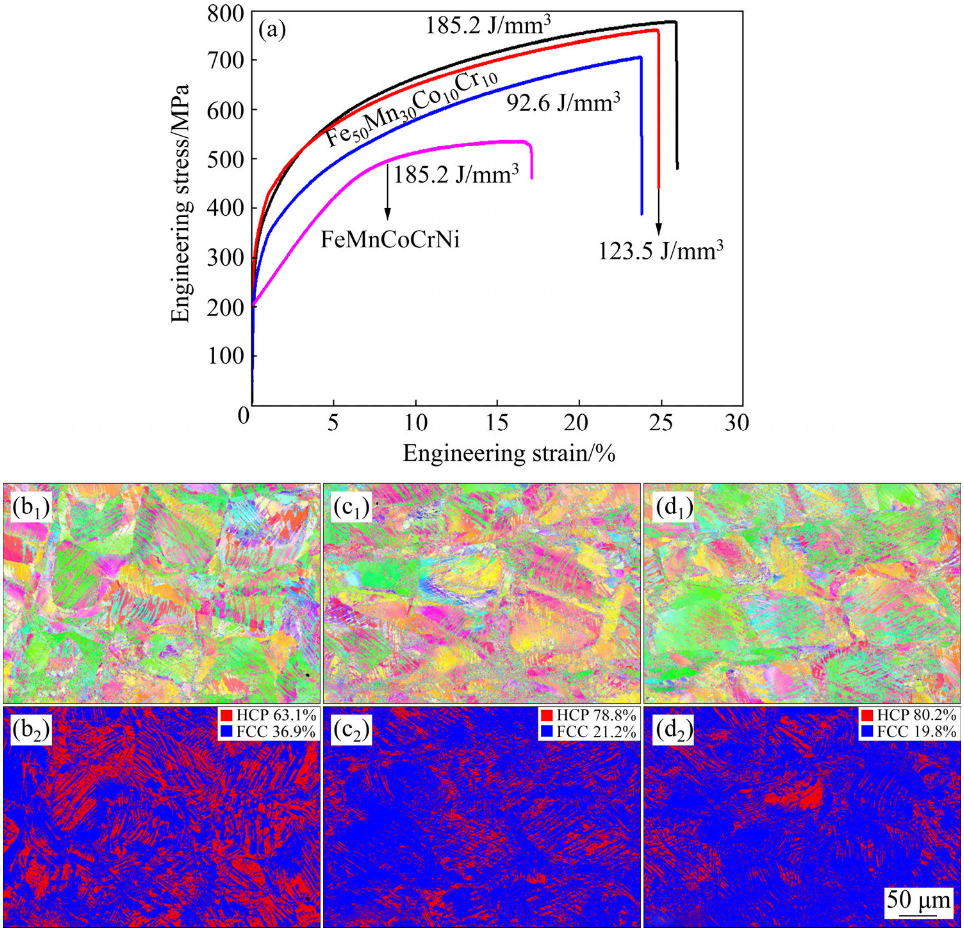

Fig. 7 Tensile engineering stress−strain curves of SLM samples at different VEDs (a), EBSD maps of SLM processed Fe$_{50}$Mn$_{30}$Co$_{10}$Cr$_{10}$ HEA at VED of 185.2 J/mm^3 with different strain levels of 20% (b$_1$), 25% (c$_1$) and 30% (d$_1$), and corresponding phase distribution maps with strain levels of 20% (b$_2$), 25% (c$_2$) and 30% (d$_2$)

tensile deformation in the printed metastable HEA.

4 Discussion

4.1 Displacive phase transformation alleviated micro-cracking

In the present work, the most intriguing finding is that the micro-cracks usually formed in the SLM processed alloys including the stable quinary FeMnCoCrNi HEA can be suppressed in the metastable non-equiatomic quaternary FeMnCoCr HEA with the displacive phase transformation from the FCC matrix to the HCP martensite. During the SLM process, residual thermal stress associated with the cooling of melted materials is inevitable and generally unfavorable for metal 3D printing, prone to inducing micro-cracks. In this regard, reducing or alleviating the residual thermal stress and the associated micro-cracking behavior during the printing process is significantly important for the performance of SLM processed materials. From the energy dissipation aspect, cracking is a dissipation route of thermal stress related internal energy in rapid solidification after laser melting; the internal energy is usually spontaneously transformed into surface energy by micro-cracking. Except for micro-cracking, the thermal stress stored energy can also be consumed by other routes. As an interesting finding, the present study shows that the thermal stress can be consumed by displacive phase transformation from the FCC matrix to the HCP martensite. However, the equimolar FeMnCoCrNi HEA does not show phase transformation during the fast cooling upon laser printing, leaving the micro-cracking as the main approach to consume the thermal stress related energy. By contrast, in the non-equimolar quaternary $Fe_{50}Mn_{30}Co_{10}Cr_{10}$ (at.%) HEA showing the FCC→HCP martensitic transformation, the micro-cracks were totally suppressed and the residual tensile stress in the stable FCC HEA was changed to compressive stress in the metastable FCC−HCP HEA (Fig. 3).

For the SLM printed alloy, there are several possible types of micro-cracking, e.g., solidification cracking, ductility dip cracking, liquation cracking, strain age cracking and cold cracking. Based on a careful identification in the present work, the main type of micro-cracking in the SLM printed equiatomic FeMnCoCrNi is strain (age) cracking under thermal stress instead of solidification cracking. This was evidenced by the fact that in the SLM printed equiatomic FeMnCoCrNi alloy (Fig. 2), an individual crack could pass through two or more melt pools [1]. Basically, laser additive manufacturing involves multiple laser scan tracks and layers, which could accumulate higher thermal stress than that from conventional laser welding performed with a single laser scan track.

It should be noted that both the micro-cracking in the stable quinary FeMnCoCrNi HEA and the displacive transformation in the metastable non-equiatomic quaternary FeMnCoCr HEA reported here took place during the cooling of the as-already solidified melt pool and the subsequent thermal cycle process (i.e., the strain aging process). The displacive transformation can occur in a wide temperature range from room temperature to ~550 °C in metastable non-equiatomic FeMnCoCr HEA to absorb external energies [52,53], thus, the micro-cracking can be prevented in a wide temperature range during strain aging process of AM.

The difference in the phase stability of the equimolar FeMnCoCrNi HEA and that of the non-equimolar $Fe_{50}Mn_{30}Co_{10}Cr_{10}$ HEA can be understood from their difference in stacking fault energy (SFE). It has been confirmed that the SFE of the non-equimolar $Fe_{50}Mn_{30}Co_{10}Cr_{10}$ HEA is lower than that of the equimolar FeMnCoCrNi HEA [48]. As evidenced in Fig. 5, the quinary FeMnCoCrNi HEA exhibits no SFs in as-printed condition while the quaternary $Fe_{50}Mn_{30}Co_{10}Cr_{10}$ HEA presents a large number of SFs. In a simple model, SFE corresponds to the energy difference between the HCP and the FCC structures [54]. The driving force of phase transformation from the FCC γ to the HCP ε mainly comes from the difference of chemistry free energy change between the parent FCC γ and the product HCP ε phases, i.e., $\Delta G^{\gamma\to\varepsilon}$. When $\Delta G^{\gamma\to\varepsilon}$ is not sufficiently low, additional driving force is necessary to trigger the transformation. In this regard, the externally applied stress and internal thermal stress can provide the necessary driving force. Thus, in the present work of SLM printing metastable $Fe_{50}Mn_{30}Co_{10}Cr_{10}$ HEA, the thermal stress during the fast cooling after laser melting transfers into beneficial merit to cause the FCC→HCP phase transformation although such thermal stress is usually detrimental for other SLM materials including the single FCC FeMnCoCrNi HEA. In this way, the displacive phase transformation in the metastable $Fe_{50}Mn_{30}Co_{10}Cr_{10}$ HEA releases the internal thermal stress during printing process, preventing crack generation and propagation. Further, the residual stress changes from tensile stress to compressive stress by FCC→HCP transformation as verified by residual stress tests (Fig. 3).

4.2 Effect of volumetric energy density on residual stress and phase transformation

As shown in Fig. 3, both the residual tensile stress in the stable equimolar FeMnCoCrNi HEA and the residual compressive stress in the metastable non-equimolar $Fe_{50}Mn_{30}Co_{10}Cr_{10}$ HEA gradually increase with the increase of VED. In fact, the higher VED, the higher melt pool temperature and the higher cooling rate, which inevitably induces much larger thermal stress [55,56]. Thus, the residual tensile stress increases with the increase of VED for the stable equimolar FeMnCoCrNi HEA. When the residual tensile stress exceeds a critical value, cracks occur inside the printed HEA sample. Further, the increase of residual tensile stress leads to more extensive cracking behavior in the stable equimolar FeMnCoCrNi HEA as confirmed in Fig. 2. For the metastable non-equimolar $Fe_{50}Mn_{30}Co_{10}Cr_{10}$ HEA, the thermal stress promotes FCC→HCP phase transformation. Therefore, the higher cooling rate at higher VED, the much higher capability to promote phase transformation as evidenced in the XRD patterns in Fig. 1. As a result, for the metastable HEA, increasing VED results in much higher volume fraction of HCP phase and accordingly a much higher residual compressive stress in the as-printed sample.

4.3 Strengthening effect of phase transformation

Other than inhibiting the micro-cracks, the FCC→HCP phase transformation occurred under internal stress during 3D printing process produces harder HCP martensite phase and thereby enhances the strength of the as-printed HEA as the phase interfaces provide effective obstacles for dislocation slip upon the subsequent deformation [53,57,58]. Also, the remaining FCC phase after 3D printing can undergo subsequent transformation to the HCP martensite under the external stress during tensile testing, further providing the strengthening effect to the printed metastable HEA. Figure 8(a) shows the

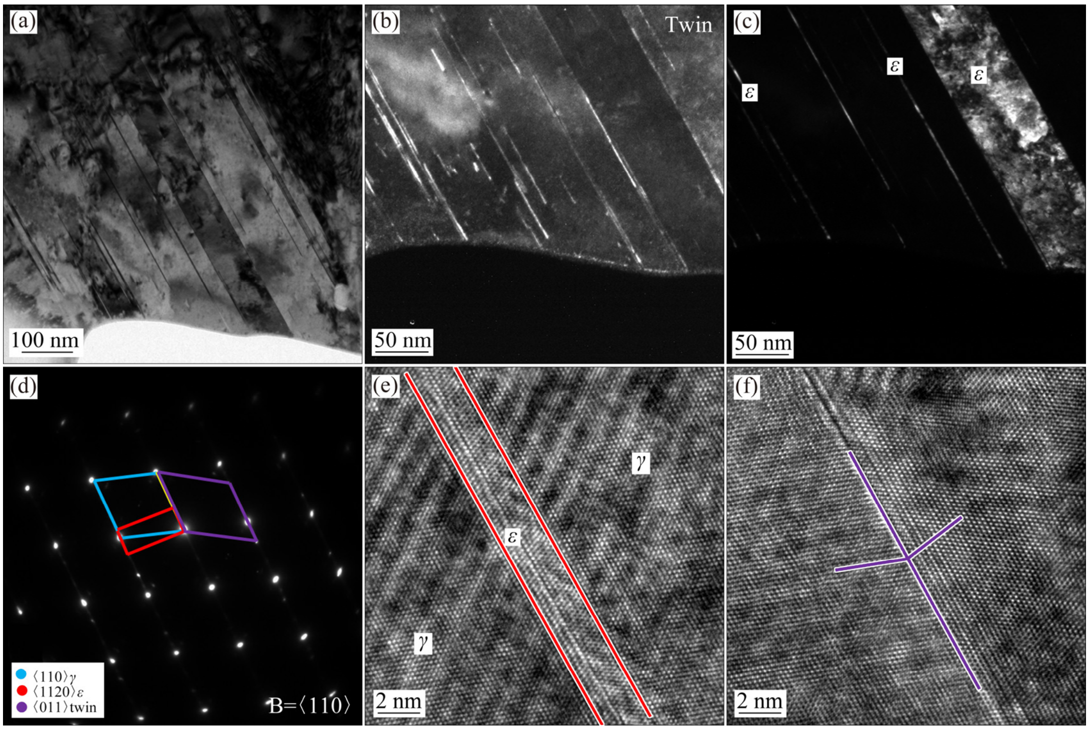

Fig. 8 TEM analysis of sample region near fracture surface in SLM processed $Fe_{50}Mn_{30}Co_{10}Cr_{10}$ HEA after tensile deformation: (a) Bright field TEM image; (b, c) Dark field TEM images of twins and HCP ε martensite, respectively; (d) SAED pattern; (e, f) HRTEM images showing HCP ε martensite and FCC twin, respectively

bright field TEM images of the sample region near to the fracture surface of the printed non-equimolar $Fe_{50}Mn_{30}Co_{10}Cr_{10}$ (at.%) HEA after tensile deformation, where a large number of dislocations can be observed. The corresponding SAED pattern shown in Fig. 8(d) suggests the coexistence of FCC matrix, HCP martensite and twin in the FCC matrix. The dark field TEM images (Figs. 8(b, c)) using different spots in the SAED pattern further confirm the presence of deformation twins and nanoscale martensite lamellae. This finding suggests that not only the FCC→HCP phase transformation can improve the mechanical property, but also the deformation twinning mechanism in the printed metastable FeMnCoCr HEA enhances the strength and ductility.

5 Conclusions

(1) The stable single FCC equiatomic FeMnCoCrNi HEA suffered from significant micro-cracking, while the metastable non-equiatomic FeMnCoCr HEA did not show micro-cracks after laser printing at various VEDs.

(2) The residual stress changes from the tensile stress in the as-printed equiatomic quinary FeMnCoCrNi HEA to compressive stress in the as-printed non-equiatomic quaternary FeMnCoCr HEA. Both the residual tensile stress in the stable equiatomic FeMnCoCrNi HEA and the residual compressive stress in the metastable non-equiatomic FeMnCoCr HEA gradually increase with the increase of VED.

(3) The displacive transformation from the FCC matrix to the HCP martensite during SLM effectively prevents the micro-cracking of the metastable HEAs via consuming thermal stress related internal energy. The higher VED, the more HCP ε martensite phase is formed and higher residual compressive stress is presented in the SLM printed non-equiatomic quaternary FeMnCoCr HEA.

(4) Except for alleviating micro-cracking, the FCC γ→HCP ε phase transformation under internal stress during 3D printing process also enhances the tensile strength of the metastable HEA by producing the harder HCP ε phase. The further displacive phase transformation from the remaining FCC matrix (after printing) to the HCP martensite during tensile deformation also contributes to the strength and ductility of the printed metastable HEA.

Acknowledgments

The authors wish to acknowledge the financial support of the National Natural Science Foundation of China (51505166, 51971248), the Huxiang Young Talents Project (2018RS3007, 2019RS1001), the Innovation-Driven Project of Central South University, China (2020CX023), and Science and Technology Project of Hunan Province (2020GK2031).

References

[1] CHAUVET E, KONTIS P, JAEGLE E A, GAULT B, RAABE D, TASSIN C, BLANDIN J J, DENDIEVEL R, VAYRE B, ABED S, MARTIN G. Hot cracking mechanism affecting a non-weldable Ni-based superalloy produced by selective electron beam melting [J]. Acta Materialia, 2018, 142: 82−94.

[2] HILAIRE A, ANDRIEU E, WU Xin-hua. High-temperature mechanical properties of alloy 718 produced by laser powder bed fusion with different processing parameters [J]. Additive Manufacturing, 2019, 26: 147−160.

[3] WANG Y M, VOISIN T, MCKEOWN J T, YE Jian-chao, CALTA N P, LI Zan, ZENG Zhi, ZHANG Yin, CHEN Wen, ROEHLING T T, OTT R T, SANTALA M K, DEPOND P J, MATTHEWS M J, HAMZA A V, ZHU Ting. Additively manufactured hierarchical stainless steels with high strength and ductility [J]. Nature Materials, 2018, 17: 63−71.

[4] GU Dong-dong, WANG Hong-qiao, DAI Dong-hua, CHANG Fei, MEINERS W, HAGEDORN Y C, WISSENBACH K, KELBASSA I, POPRAWE R. Densification behavior, microstructure evolution, and wear property of TiC nanoparticle reinforced AlSi10Mg bulk-form nanocomposites prepared by selective laser melting [J]. Journal of Laser Applications, 2015, 271: S17003.

[5] HARRISON N J, TODD I, MUMTAZ K. Reduction of micro-cracking in nickel superalloys processed by selective laser melting: A fundamental alloy design approach [J]. Acta Materialia, 2015, 94: 59−68.

[6] KUMAR P, PRAKASH O, RAMAMURTY U. Micro-and meso-structures and their influence on mechanical properties of selectively laser melted Ti−6Al−4V [J]. Acta Materialia, 2018, 154: 246−260.

[7] LI J F, LI L, STOTT F H. Thermal stresses and their implication on cracking during laser melting of ceramic materials [J]. Acta Materialia, 2004, 52: 4385−4398.

[8] GARIBALDI M, ASHCROFT I, SIMONELLI M, HAGUE R. Metallurgy of high-silicon steel parts produced using Selective Laser Melting [J]. Acta Materialia, 2016, 110: 207−216.

[9] RUTTERT B, RAMSPERGER M, RONCERY L M, LOPEZ G I, KOERNER C, THEISEN W. Impact of hot isostatic pressing on microstructures of CMSX-4 Ni-base superalloy

fabricated by selective electron beam melting [J]. Materials & Design, 2016, 110: 720−727.

[10] JOSEPH J, HODGSON P, JARVIS T, WU Xin-hua, STANFORD N, FABIJANIC D M. Effect of hot isostatic pressing on the microstructure and mechanical properties of additive manufactured Al*x*CoCrFeNi high entropy alloys [J]. Materials Science and Engineering A, 2018, 733: 59−70.

[11] WANG Fu-de. Mechanical property study on rapid additive layer manufacture Hastelloy ® X alloy by selective laser melting technology [J]. International Journal of Advanced Manufacturing Technology, 2012, 58: 545−551.

[12] PARRY L, ASHCROFT I A, WILDMAN R D. Understanding the effect of laser scan strategy on residual stress in selective laser melting through thermo-mechanical simulation [J]. Additive Manufacturing, 2016, 12: 1−15.

[13] COSTA M M, DANTAS T A, BARTOLOMEU F, ALVES N, SILVA F S, MIRANDA G, TOPTAN F. Corrosion behaviour of PEEK or β-TCP-impregnated Ti6Al4V SLM structures targeting biomedical applications [J]. Transactions of Nonferrous Metals Society of China, 2019, 29: 2523−2533.

[14] VRANCKEN B, CAIN V, KNUTSEN R, van HUMBEECK J. Residual stress via the contour method in compact tension specimens produced via selective laser melting [J]. Scripta Materialia, 2014, 87: 29−32.

[15] SAEDI S, MOGHADDAM N S, AMERINATANZI A, ELAHINIA M, KARACA H E. On the effects of selective laser melting process parameters on microstructure and thermomechanical response of Ni-rich NiTi [J]. Acta Materialia, 2018, 144: 552−560.

[16] SATO Y, TSUKAMOTO M, SHOBU T, YAMASHITA Y, YAMAGATA S, NISHI T, HIGASHINO R, OHKUBO T, NAKANO H, ABE N. Preheat effect on titanium plate fabricated by sputter-free selective laser melting in vacuum [J]. Applied Physics A: Materials Science and Processing, 2018, 124: 288.

[17] LI Wei, LIU Jie, ZHOU Yan, WEN Shi-feng, WEI Qing-song, YAN Chun-ze, SHI Yu-sheng. Effect of substrate preheating on the texture, phase and nanohardness of a Ti−45Al−2Cr−5Nb alloy processed by selective laser melting [J]. Scripta Materialia, 2016, 118: 13−18.

[18] SCHEITLER C, HENTSCHEL O, KREBS T, NAGULIN K Y, SCHMIDT M. Laser metal deposition of NiTi shape memory alloy on Ti sheet metal: Influence of preheating on dissimilar build-up [J]. Journal of Alloys and Compound, 2017, 29: 022309.

[19] SISTIAGA M L M, MERTENS R, VRANCKEN B, WANG Xie-bin, van HOOREWEDER B, KRUTH J P, van HUMBEECK J. Changing the alloy composition of A17075 for better processability by selective laser melting [J]. Journal of Materials Processing Technology, 2016, 238: 437−445.

[20] GLODEŽ S, KLEMENC J, ZUPANIČ F, VESENJAK M. High-cycle fatigue and fracture behaviours of SLM AlSi10Mg alloy [J]. Transactions of Nonferrous Metals Society of China, 2020, 30: 2577−2589.

[21] LI Lan-bo, LI Rui-di, YUAN Tie-chui, CHEN Chao, ZHANG Zhi-jian, LI Xiao-feng. Microstructures and tensile properties of a selective laser melted Al−Zn−Mg−Cu (Al7075) alloy by Si and Zr microalloying [J]. Materials Science and Engineering A, 2020, 787: 139492.

[22] WANG Pei, ECKERT J, PRASHANTH K G, WU Ming-wei, KABAN I, XI Li-xia, SCUDINO S. A review of particulate-reinforced aluminum matrix composites fabricated by selective laser melting [J]. Transactions of Nonferrous Metals Society of China, 2020, 30: 2001−2034.

[23] MARTIN J H, YAHATA B D, HUNDLEY J M, MAYER J A, SCHAEDLER T A, POLLOCK T M. 3D printing of high-strength aluminium alloys [J]. Nature, 2017, 549: 365−369.

[24] CROTEAU J R, GRIFFITHS S, ROSSELL M D, LEINENBACH C, KENEL C, JANSEN V, SEIDMAN D N, DUNAND D C, VO N Q. Microstructure and mechanical properties of Al−Mg−Zr alloys processed by selective laser melting [J]. Acta Materialia, 2018, 153: 35−44.

[25] LI Zhi-ming, KORMANN F, GRABOWSKI B, NEUGEBAUER J, RAABE D. Ab initio assisted design of quinary dual-phase high-entropy alloys with transformation-induced plasticity [J]. Acta Materialia, 2017, 136: 262−270.

[26] OTTO F, DLOUHY A, SOMSEN Ch, BEI H, EGGELER G, GEORGE E P. The influences of temperature and microstructure on the tensile properties of a CoCrFeMnNi high-entropy alloy [J]. Acta Materialia, 2013, 61: 5743−5755.

[27] YEH J W, CHEN S K, LIN S J, GAN J Y, CHIN T S, SHUN T T, TSAU C H, CHANG S Y. Nanostructured high-entropy alloys with multiple principal elements: Novel alloy design concepts and outcomes [J]. Advanced Engineering Materials, 2004, 6: 299−303.

[28] CANTOR B, CHANG I T H, KNIGHT P, VINCENT A J B. Microstructural development in equiatomic multicomponent alloys [J]. Materials Science and Engineering A, 2004, 375: 213−218.

[29] BONISCH M, WU Y, SEHITOGLU H. Hardening by slip-twin and twin-twin interactions in FeMnNiCoCr [J]. Acta Materialia, 2018, 153: 391−403.

[30] MA Xiao-guang, CHEN Jian, WANG Xian-hui, XU Yan-jin, XUE Yu-jie. Microstructure and mechanical properties of cold drawing CoCrFeMnNi high entropy alloy [J]. Journal of Alloys and Compound, 2019, 795: 45−53.

[31] LAPLANCHE G, GADAUD P, PERRIERE L, GUILLOT I, COUZINIE J P. Temperature dependence of elastic moduli in a refractory HfNbTaTiZr high-entropy alloy [J]. Journal of Alloys and Compound, 2019, 799: 538−545.

[32] CAI Y P, WANG G J, MA Y J, CAO Z H, MENG X K. High hardness dual-phase high entropy alloy thin films produced by interface alloying [J]. Scripta Materialia, 2019, 162: 281−285.

[33] GLUDOVATZ B, HOHENWARTER A, CATOOR D, CHANG E H, GEORGE E P, RITCHIE R O. A fracture-resistant high-entropy alloy for cryogenic applications [J]. Science, 2014, 345: 1153−1158.

[34] LUO Hong, LI Zhi-ming, RAABE D. Hydrogen enhances strength and ductility of an equiatomic high-entropy alloy [J]. Scientific Reports, 2017, 7: 9892.

[35] LUO Hong, LU Wen-jun, FANG Xu-fei, PONGE D, LI Zhi-ming, RAABE D. Beating hydrogen with its own weapon: Nano-twin gradients enhance embrittlement

resistance of a high-entropy alloy [J]. Materials Today, 2018, 21: 1003−1009.

[36] ZHAO Xiao, SONG Bo, FAN Wen-rui, ZHANG Yuan-jie, SHI Yu-sheng. Selective laser melting of carbon/AlSi10Mg composites: Microstructure, mechanical and electronical properties [J]. Journal of Alloys and Compound, 2016, 665: 271−281.

[37] LI R D, YUAN T C, WEI Q S, WANG L, SHI Y S. Effects of thermal history and isostatic pressing on the microstructure evolution of metallic components manufactured by selective laser melting (SLM) [J]. Laser in Engineering, 2013, 25: 23−38.

[38] LI Bo, ZHANG Lei, XU Yi, LIU Zhi-yuan, QIAN Bo, XUAN Fu-zhen. Selective laser melting of CoCrFeNiMn high entropy alloy powder modified with nano-TiN particles for additive manufacturing and strength enhancement: Process, particle behavior and effects [J]. Powder Technology, 2020, 360: 509−521.

[39] SU Yue, LUO Shun-cun, WANG Ze-min. Microstructure evolution and cracking behaviors of additively manufactured Al*x*CrCuFeNi2 high entropy alloys via selective laser melting [J]. Journal of Alloys and Compound, 2020, 842: 155823.

[40] ZHANG Cheng-cheng, FENG Kai, KOKAWA H, HAN Bo-lun, LI Zhu-guo. Cracking mechanism and mechanical properties of selective laser melted CoCrFeMnNi high entropy alloy using different scanning strategies [J]. Materials Science and Engineering A, 2020, 789: 139672.

[41] LI Rui-di, NIU Peng-da, YUAN Tie-chui, CAO Peng, CHEN Chao, ZHOU Ke-chao. Selective laser melting of an equiatomic CoCrFeMnNi high-entropy alloy: Processability, non-equilibrium microstructure and mechanical property [J]. Journal of Alloys and Compound, 2018, 746: 125−134.

[42] LUO Shun-cun, GAO Piao, YU Han-chen, YANG Jing-jing, WANG Ze-min, ZENG Xiao-yan. Selective laser melting of an equiatomic AlCrCuFeNi high-entropy alloy: Processability, non-equilibrium microstructure and mechanical behavior [J]. Journal of Alloys and Compound, 2019, 771: 387−397.

[43] ZHANG Mi-na, ZHOU Xiang-lin, WANG Da-feng, ZHU Wu-zhi, LI Jing-hao, ZHAO Y F. AlCoCuFeNi high-entropy alloy with tailored microstructure and outstanding compressive properties fabricated via selective laser melting with heat treatment [J]. Materials Science and Engineering A, 2019, 743: 773−784.

[44] SUN Z, TAN X P, DESCOINS M, MANGELINCK D, TOR S B, LIM C S. Revealing hot tearing mechanism for an additively manufactured high-entropy alloy via selective laser melting [J]. Scripta Materialia, 2019, 168: 129−133.

[45] NIU Peng-da, LI Rui-di, ZHU Shu-ya, WANG Min-bo, CHEN Chao, YUAN Tie-chui. Hot cracking, crystal orientation and compressive strength of an equimolar CoCrFeMnNi high-entropy alloy printed by selective laser melting [J]. Optics and Laser Technology, 2020, 127: 106147.

[46] LUO Shun-cun, ZHAO Chun-yang, SU Yue, LIU Qi, WANG Ze-min. Selective laser melting of dual phase AlCrCuFeNi*x* high entropy alloys: Formability, heterogeneous microstructures and deformation mechanisms [J]. Additive Manufacturing, 2020, 31: 100925.

[47] WANG Yin, LI Rui-di, NIU Peng-da, ZHANG Zhi-jian, YUAN Tie-chui, YUAN Ji-wei, LI Kun. Microstructures and properties of equimolar AlCoCrCuFeNi high-entropy alloy additively manufactured by selective laser melting [J]. Intermetallics, 2020, 120: 106746.

[48] LI Zhi-ming, RAABE D. Strong and ductile non-equiatomic high-entropy alloys: Design, processing, microstructure, and mechanical properties [J]. JOM, 2017, 69: 2099−2106.

[49] LI Zhi-ming, PRADEEP K G, DENG Yun, RAABE D, TASAN C C. Metastable high-entropy dual-phase alloys overcome the strength–ductility trade-off [J]. Nature, 2016, 534: 227−230.

[50] DI GIOVANNI M T, de MENEZES J T O, BOLELLI G, CERRI E, CASTRODEZA E M. Fatigue crack growth behavior of a selective laser melted AlSi10Mg [J]. Engineering Fracture Mechanics, 2019, 217: 106564.

[51] RAI A K, BISWAL R, GUPTA R K, SINGH R, RAI S K, RANGANATHAN K, GANESH P, KAUL R, BINDRA K S. Study on the effect of multiple laser shock peening on residual stress and microstructural changes in modified 9Cr−1Mo (P91) steel [J]. Surface and Coating Technology, 2019, 358: 125−135.

[52] LU Wen-jun, LIEBSCHER C, DEHM G, RAABE D, LI Zhi-ming. Bidirectional transformation enables hierarchical nanolaminate dual-phase high-entropy alloys [J]. Advanced Materials, 2018, 30: 1804727.

[53] SU Jing, WU Xiao-xiang, RAABE D, LI Zhi-ming. Deformation-driven bidirectional transformation promotes bulk nanostructure formation in a metastable interstitial high entropy alloy [J]. Acta Materialia, 2019, 167: 23−39.

[54] ISHIDA K. Direct estimation of stacking fault energy by thermodynamic analysis [J]. Physica Status Solidi (a), 1976, 36: 717−728.

[55] SALEM M, ROUX S L, HOR A, DOUR G. A new insight on the analysis of residual stresses related distortions in selective laser melting of Ti−6Al−4V using the improved bridge curvature method [J]. Additive Manufacturing, 2020, 36: 101586.

[56] LI Rui-di, WANG Min-bo, LI Zhi-ming, CAO Peng, YUAN Tie-chui, ZHU Hong-bin. Developing a high-strength Al−Mg−Si−Sc−Zr alloy for selective laser melting: Crack-inhibiting and multiple strengthening mechanisms [J]. Acta Materialia, 2020, 193: 83−98.

[57] LI Zhi-ming, RAABE D. Influence of compositional inhomogeneity on mechanical behavior of an interstitial dual-phase high-entropy alloy [J]. Materials Chemistry and Physics, 2018, 210: 29−36.

[58] SU Jing, RAABE D, LI Zhi-ming. Hierarchical microstructure design to tune the mechanical behavior of an interstitial TRIP-TWIP high-entropy alloy [J]. Acta Materialia, 2019, 163: 40−54.

增材制造高强韧高熵合金中
基于切变型相变的微裂纹抑制机理

李瑞迪[1]，牛朋达[1]，袁铁锤[1]，李志明[1,2]

1. 中南大学 粉末冶金国家重点实验室，长沙 410083；
2. 中南大学 材料科学与工程学院，长沙 410083

摘　要：研究选区激光熔化增材制造 FeMnCoCrNi 体系高熵合金的微裂纹行为，并采用 XRD 技术对激光打印后样品表面的残余应力进行分析。结果表明，经激光打印后等原子比 FeMnCoCrNi 高熵合金显示为稳定的单相面心立方(FCC)结构，出现残余拉应力，并产生微裂纹。相比之下，具有低层错能的非等原子比亚稳 FeMnCoCr 高熵合金在各种激光能量密度下均出现残余压应力，且无微裂纹形成。在激光熔化后的冷却过程中，亚稳高熵合金中发生的从 FCC 基体相到密排六方(HCP)相的切变型相变消耗了激光打印过程中的热应力，从而抑制微裂纹的产生。此外，相比于单相稳定高熵合金，亚稳高熵合金在拉伸变形过程中马氏体相变也有助于提高其抗拉强度和延展性。这些结果为增材制造领域设计开发高强、高韧、无裂纹的合金提供有益参考。

关键词：选区激光熔化；高熵合金；相变；微裂纹；残余应力

(Edited by Xiang-qun LI)